Frequency-Domain Optical Tomographic Imaging of Arthritic Finger Joints

Andreas H. Hielscher*, *Member, IEEE*, Hyun Keol Kim, Ludguier D. Montejo, *Member, IEEE*, Sabine Blaschke, Uwe J. Netz, Paul A. Zwaka, Gerd Illing, Gerhard A. Müller, and Jürgen Beuthan

***Abstract*—We are presenting data from the largest clinical trial on optical tomographic imaging of finger joints to date. Overall we evaluated 99 fingers of patients affected by rheumatoid arthritis (RA) and 120 fingers from healthy volunteers. Using frequency-domain imaging techniques we show that sensitivities and specificities of 0.85 and higher can be achieved in detecting RA. This is accomplished by deriving multiple optical parameters from the optical tomographic images and combining them for the statistical analysis. Parameters derived from the scattering coefficient perform slightly better than absorption derived parameters. Furthermore we found that data obtained at 600 MHz leads to better classification results than data obtained at 0 or 300 MHz.**

***Index Terms*—Computer aided diagnostics, light propagation in tissue, optical tomography, rheumatoid arthritis (RA).**

I. Introduction

OVER the last decade several groups have pursued the use of optical tomographic methods to image arthritis and other joint diseases. Jiang *et al.* have performed extensive studies to show the potential of optical tomography to detect osteoarthritis (OA). In 2001 they introduced a continuous-wave (CW) system for reconstructing absorption and scattering coefficients of joints [1]. Using experimental data from a human finger and several chicken bones, this group subsequently showed that 3-D volumetric reconstructions can provide details of the joint structure and composition that would be impossible from 2-D imaging methods [2]. For this study they employed a finite-element algorithm that was based on the diffusion equation of light transport in tissue. Refining the imaging hardware and software further, they presented first clinical results involving data from two OA patients and three healthy volunteers in 2007 [3]–[5]. They found that the reconstructed images demonstrated differences in optical properties in the joint region between the OA and healthy joints. Since then this group has further improved their system by introducing a combined X-ray optical-imaging system [6], developed a new instrument based on photo-acoustic imaging [7], and moved beyond the diffusion model to include higher-order reconstruction schemes that account for light-transport effects not previously covered [8]. The X-ray system was used to image the distal inter-phalangeal (DIP) joints of 22 patients and 18 healthy volunteers, while the photo-acoustic system was explored by imaging DIP joints of 2 OA patients and four healthy subjects. In 2007, Wang *et al.* showed the potential of photo-acoustic tomography (PAT) for imaging of human peripheral joints by studying the method's resolution in cadaver human fingers and small animals [9], [10]. More recently, several researchers have suggested molecular imaging approaches that involved bioluminescence and fluorescence markers [11]–[13]. However, they did not apply tomographic imaging methods.

Our research team has focused in the past on application of optical tomographic imaging for detecting and characterizing inflammation in rheumatoid arthritis (RA). RA is an autoimmune disease characterized by chronic inflammation of the synovial membrane of joints [14], [15]. The etiology of RA is unknown, however, it affects an estimated 1.5 million Americans. Patients with RA can suffer from crippling pain and lack of joint mobility. These handicaps can result in large financial costs due to health care expenses and loss of productivity at work. Despite recent advances in therapeutic intervention including biological therapies, there is currently no cure of RA. However, early treatment of RA has been shown to significantly improve clinical outcome and management of the disease. It is therefore important to diagnose a patient with RA as early as possible.

In previous studies we showed that the absorption coefficients μ_a inside the joint cavity are elevated in patients with RA compared to healthy subjects [16]–[18]. However, using just a single parameter [for example, the smallest or the largest absorption coefficient, $\min(\mu_a)$ or $\max(\mu_a)$] for classification, sensitivities (Se) and specificities (Sp) of only 0.71 were achieved. Subsequently, Klose *et al.* [19], showed that if optically derived parameters, such as $\min(\mu_a)$ and and $\max(\mu_a)$, are combined for the classification process, sensitivities and specificities can be increased to 0.76 and 0.78, respectively.

Manuscript received February 06, 2011; accepted March 08, 2011. Date of publication April 05, 2011; date of current version September 30, 2011. This work was supported in part by a grant from the National Institute of Arthritis and Musculoskeletal and Skin Diseases (NIAMS-2R01 AR46255), which is part of the National Institutes of Health. *Asterisk indicates corresponding author.*

*A. H. Hielscher is with the Departments of Biomedical Engineering, Radiology, and Electrical Engineering, Columbia University, New York, 10027 USA (e-mail: ahh2004@columbia.edu).

H. K. Kim and L. D. Montejo are with the Department of Biomedical Engineering, Columbia University, New York 10027 USA (e-mail: hkk2107@columbia.edu; ldm2106@columbia.edu).

S. Blaschke and G. A. Müller are with the Department of Nephrology and Rheumatology, Georg-August-University, University Medical Center Göttingen, 37075 Göttingen, Germany.

U. J. Netz is with the Laser- und Medizin-Technologie GmbH Berlin, 14195 Berlin-Dahlem, Germany and with the Department of Medical Physics and Laser Medicine, Charité-Universitätsmedizin Berlin, 10117 Berlin, Germany.

P. A. Zwaka is with the Department of Radiology, Georg-August-University, University Medical Center Göttingen, 37075 Göttingen, Germany.

G. Illing is with Laser- und Medizin-Technologie GmbH Berlin, 14195 Berlin-Dahlem, Germany.

J. Beuthan is with the Department of Medical Physics and Laser Medicine, Charité-Universitätsmedizin Berlin, 10117 Berlin, Germany.

Color versions of one or more of the figures in this paper are available online at http://ieeexplore.ieee.org.

Digital Object Identifier 10.1109/TMI.2011.2135374

In these previous studies a continuous wave (CW) instrument was used that measured the amplitude of transmitted light intensities. However, it is known that CW systems have difficulties separating absorption and scattering effects, which may limit the achievable sensitivities and specificities. In this work we present first clinical results obtained with a frequency-domain imaging system. In addition to amplitude information, frequency-domain data contains phase information, which has been shown to improve the separation of scattering and absorption effects [20]. By imaging over 200 fingers at three different modulation frequencies (0, 300, and 600 MHz) and comparing the results to established clinical criteria, ultrasound (US) and magnetic resonance imaging (MRI), we sought to demonstrate that frequency-domain imaging leads to higher sensitivities and specificities. Furthermore, by combining a multitude of optically derived parameters, we explored the possibility of using computer aided diagnostic tools that could assist in the diagnosis of rheumatoid arthritis.

II. Patients and Methods

A. Introduction

In this study 36 patients, previously diagnosed with rheumatoid arthritis (RA), were enrolled at the Department of Nephrology and Rheumatology, University Medicine of Göettingen, Germany. Data from three patients was discarded because the optical tomographic imaging system failed to operate correctly during the exam. Of the remaining 33 RA patients, 24 were female and 9 male, which reflects the fact that RA is 2–3 times more common in women than in men. The mean age of these patients was 51.5 ± 13.9 years (range 21–77 years). All patients met the criteria for the diagnosis of RA established by the American College of Rheumatology (ACR) and the European League Against Rheumatism (EULAR) [21], [22]. Most of the patients (21/33; 63.6%) received standard disease-modifying anti-rheumatic drug therapy (methotrexate, leflunomide, adalimumab) and low-dose prednisone ($<$10 mg/d). Positivity for the rheumatoid factor was found in 8 out of 33 cases (24%). All patients had active disease, defined as at least three swollen and tender peripheral joints and morning stiffness for $>$1 hour, with or without an elevated erythrocyte sedimentation rate $(\mathrm{ESR} > 28$ mm/h) or C-reactive protein level $(\mathrm{CRP} > 8$ mg/l). The mean clinical disease activity, assessed according to the method previously defined by van der Heijde *et al.* [23], was 4.6 (range 1.59–8.02).

All patients were subjected to clinical examination (CE), ultrasound (US) imaging and low-field MRI of the clinically predominant hand. Furthermore, proximal interphalangeal (PIP) joints II-IV were subjected to frequency-domain optical tomography (FDOT), resulting in 99 images of fingers from RA patients. As controls 20 healthy persons $(\mathrm{male{:}female} = 6:14)$ with a mean age of 38.8 ± 14.1 years (range 22–60 years) were included and subjected to FDOT analysis of PIP joints II–IV of both hands (resulting in $2 \times 20 \times 3 = 120$ FDOT images of healthy finger joints). The study was approved by the Institutional Review Board (IRB) and each patient and healthy control gave informed consent prior to study entry.

B. Gold Standard

To establish a gold standard for classification results CE, MRI, and US were used to determine if a finger was affected by RA or not. The CE of each PIP joint was performed by bi-manual palpation to assess the degree of swelling, tenderness and warmth. The joints were classified according to a clinical synovitis score (CSS) [24], [25]. To assess the overall state of the disease, laboratory tests included the erythrocyte sedimentation rate (ESR) and C-reactive protein (CRP). Both blood tests used to detect inflammation within the body. Higher sedimentation rates indicate the presence of inflammation and occur in inflammatory disease, such as RA. The CRP is a protein built in liver tissue and also considered a parameter of inflammation as part of activating the immune system. Although not specific, both parameters show a good correlation to RA disease activity. Finally, an overall disease activity score (DAS) was assessed as part of the clinical exam. The DAS28 is a combined index that has been developed to measure the disease activity in patients with RA [26], [27]. It includes a classification of 28 joints according to the degree of swelling and tenderness, the ESR, and a patient self-assessment according to the visual analogue scale (VAS). The DAS28 results in a number between 0 and 10, indicating how active the RA is at this moment. Using the DAS28, several thresholds have been developed for high disease activity, low disease activity, or disease inactivity. Disease activity is defined as inactive when $\mathrm{DAS28} < 3.2$, moderately active if $3.2 < \mathrm{DAS28} < 5.1$ and highly active if $\mathrm{DAS28} > 5.1$.

MRI was performed using a dedicated low-field (0.2 T) MRI system (C-scan, ESAOTE, Genova, Italy) equipped with a specifically designed hand coil. Imaging sequences included native gradient-echo short-tau inversion-recovery (STIR) sequence in coronal slice orientation, T1-weighted spin-echo high resolution sequence in transversal and coronal orientations, and T1-weighted 3-D gradient-echo sequence in coronal slice orientation before and after bolus administration of the paramagnetic contrast medium gadolinium diethylenetriaminepentaacetic acid (Gd-DTPA, Magnevist, Schering, Berlin, Germany) at a dose of 0.2 mmol/kg body weight. The data set acquired with the T1-weighted 3-D gradient echo sequence was used for reconstruction of axial views. Examples are shown in Fig. 1, which display how synovitis [Fig. 1(a) and (b)] and joint erosions [Fig. 1(c) and (d)] appear in MR images before and after administration of the contrast agent. Synovitis is clearly apparent in the contrast-enhanced image, while erosion is visible even before the administration of a Gd-DTPA bolus. Scoring of synovitis and erosions was performed according to the EULAR OMERACT criteria [24], using a semi-quantitative scoring system as previously described by Schirmer *et al.* [25].

Ultrasound imaging (US) was performed with an Esaote Technos MPX ultrasound system. We used a 14-8 MHz hockey stick linear array transducer for examination of the PIP joints. Examples of US images taken from the palmar side are shown in Fig. 2. A healthy joint is shown in Fig. 2(a), while Fig. 2(b)–(d) show joints with inflammation. In US, two criteria of active inflammation were evaluated following Szkudlarek *et al.* [28]. Joint effusion (E) was visible as an anechoic area between the capsule and the bone in the proximal part from the palmar side

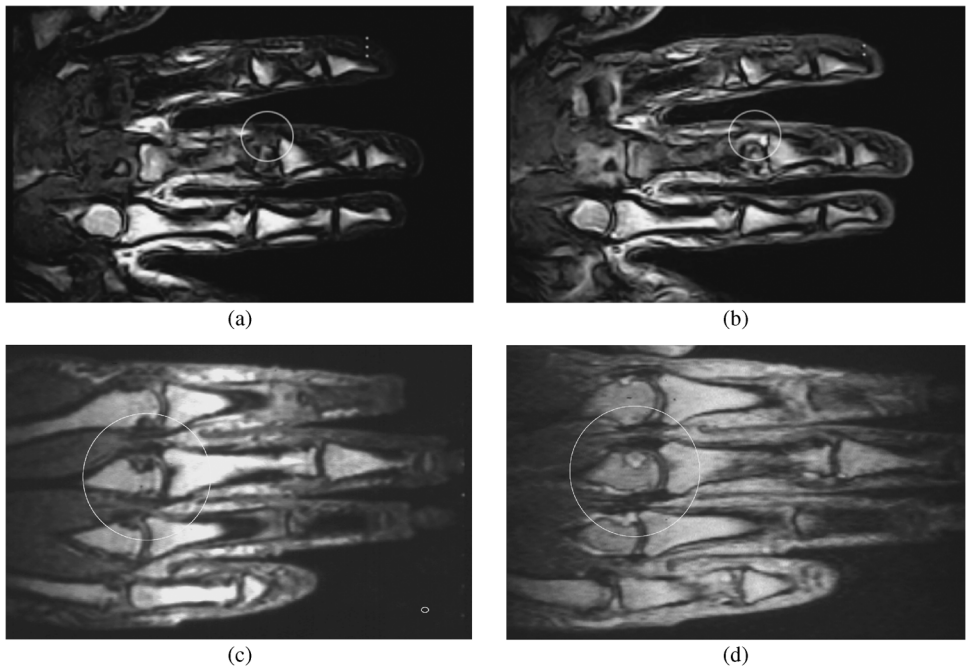

Fig. 1. (a), (b) The two figures show T1-weighted images (a) before and (b) after administration of a bolus of Gd-DTPA. The region marked with a white circle shows synovitis in a PIP joint. (c), (d) The two figures show T1-weighted images (c) before and (d) after administration of a bolus of Gd-DTPA. The region marked with a white circle shows erosions in all three joints inside the circle.

of the hand [Fig. 2(b)–(d)]. Second, thickening of the synovial membrane (S, synovitis) could be visualized as hyper-echoic structures within the region affected by effusion [Fig. 2(d)]. We performed US from palmar because we found that synovitis and effusion can best be evaluated from the palmar as opposed to the dorsal side. This is probably due to the small amount of tissue overlying the joint from the dorsal side.

MRI and US images of patients with RA were analyzed by two independent investigators including a radiologist and a rheumatologist. According to US and MRI findings, PIP joints were classified into joints affected by RA (Group A) and joints unaffected by RA (Group U). To be classified as affected by RA, joints had to show either signs of effusion, synovitis or erosions. Joints classified as unaffected by RA did not show any of these signs. In almost all cases consensus was reached in classification results. In the few case of discrepant evaluations of the two initial reviewers a third reviewer was consulted and his finding was used to determine group membership. This classification was used as ground truth for the evaluation of the frequency-domain optical tomography (FDOT) images.

C. Optical Tomographic Imaging

1) Optical Tomographic Instrument: As optical imaging system we employed a recently developed frequency-domain system that allows for source-modulation frequencies up to 1 GHz [29]. A laser beam (wavelength $\lambda = 670$ nm, optical power $= 8\,\mathrm{mW}$, beam diameter 1.0 mm) was directed onto the back of a finger and scanned across the PIP joint in a sagittal plane (Fig. 3). Transmitted light intensities were measured with an intensified CCD (ICCD) camera. The ICCD camera was operated in homodyne mode, i.e., the gain of the ICCD is modulated by a slave signal generator at the same frequency as the laser. As a result, a steady state image at the intensifier output is imaged to the CCD. The signal in every pixel depends on the phase between source and detector modulation. Master and slave signal generators are linked together and the phase delay is adjustable. To detect the complete oscillation of the modulation multiple images are taken at phase delays covering the range of 2π and are transferred to a computer. From the stack of images 2-D amplitude and phase images are derived by data processing. More details concerning this setup can be found in [29].

In addition to the transmission measurements, accurate surface coordinates of the finger were generated by a newly introduced laser scanner unit. The finger was scanned simultaneously by two red laser lines (wavelength $\lambda = 650$ nm, optical power $= 5\,\mathrm{mW}$, line width $= 0.2$ mm) at the back and the palm (Fig. 4). In this setup the diode lasers are mounted on a gear-wheel each. Slight rotation of the gear-wheel by a stepping motor yields a step of the laser line on the finger surface. Both gear-wheels are driven by one stepping motor to accomplish simultaneous scanning of the two lines. The shapes of the deformed laser lines on the finger surface are imaged with a fast video camera (SPC 900 NC, Philips, The Netherlands), which is controlled by the DAVID laser-scanner software (ver. 1.6b, TU-Braunschweig, Germany). Two thin walls besides the finger arranged in certain angle serve as calibration background to adjust the coordinate system of the camera. According to the camera coordinate system the line shapes are transformed into 3-D surface coordinates in real-time. These coordinates were employed to generate a surface mesh of the scanned part of the finger using GID software package (Micromechatornics Inc. http://www.mmech.com/) [Fig. 4(b)], which is input into the reconstruction procedure together with the transmission data. Test on standard surface phantoms showed that this setup can resolve surface details with an accuracy of at least 0.4 mm. Both the tomographic unit and the laser-scanning unit are equipped with

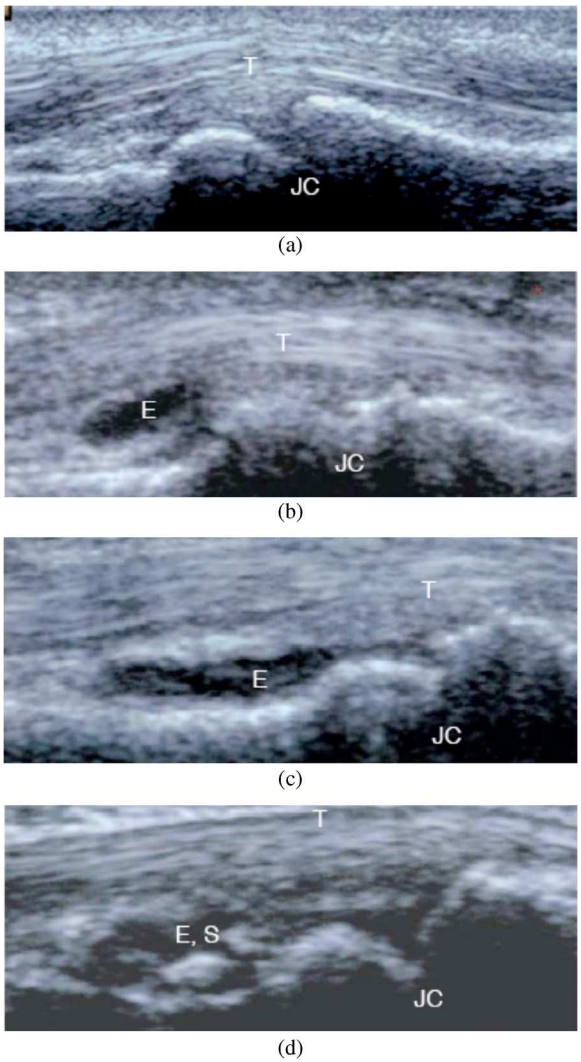

Fig. 2. Ultrasound images of a healthy joint (a), and joints affected by RA (b), (c), (d). The larger the anechoic area and/or extent of synovial hypertrophy, the higher was the ultrasound score (USS) (USS = 1 minimal, USS = 2 moderate, USS = 3 extensive effusion/hypertrophy). Images were produced by placing a hockey stick linear array transducer on the palmar side of the PIP joint. (E = effusion, S = synovitis, T = tendon, JC = joint cavity).

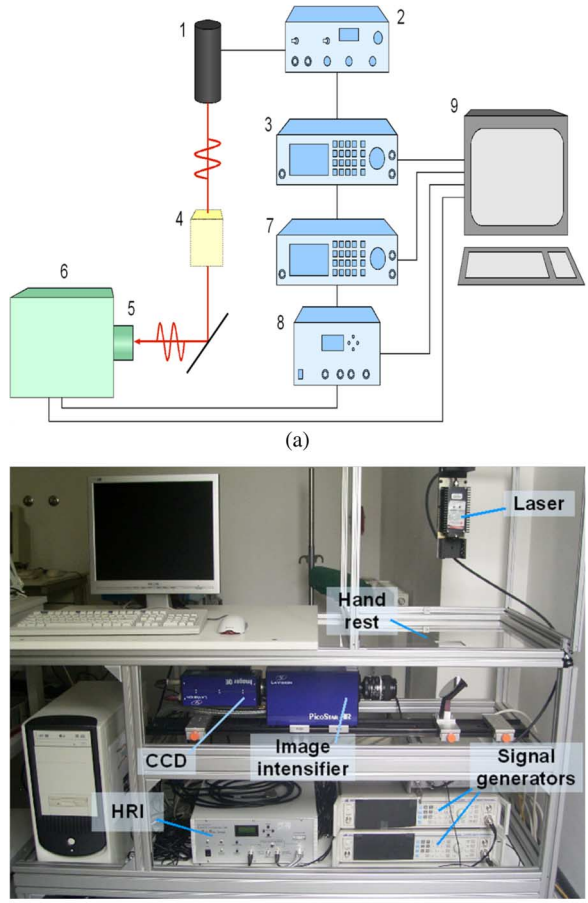

Fig. 3. Setup of tomographic scanning unit, (a) schematic and (b) photograph. The hardware parts shown are the (1) laser diode, (2) laser diode driver, (3,7) signal generator, (4) finger, (5) focusing lens, (6) ICCD camera, (8) high rate imager, and (9) computer.

identical, ergonomic hand and arm rest in the same height to allow for identical positioning of the patient's arm and hand.

2) Optical Imaging Protocol: Before the measurement was started, the fingers were marked with a small black dot on the back of the finger in the sagittal plane, 17 mm distal from the PIP joint. This mark was used to position the finger identically in both the tomographic and laser scanner unit. Once the finger was placed inside the tomographic unit on a hand rest, the laser beam was moved to the marked position. The finger axis was aligned with the scanning plane of the laser. Then, the laser moved to the first tomographic source position, 10 mm distal from the PIP joint and subsequently scanned over a range of 20 mm. Images were acquired at 11 equally spaced source positions. At every source position the oscillation was sampled in 16 phase steps with an exposure time of 80 ms each. The scan was performed twice, at first in the forward direction with modulation frequency of 600 MHz, and then in the reverse direction with a frequency of 300 MHz.

We scanned three fingers from the hand of each patient; the index, middle, and the ring finger (PIP II to PIP IV). To avoid movement artifacts in the image reconstruction, the examiner controlled the correct position of the finger again after the tomographic scan was finished. Acquisition time for one finger including laser movement, image acquisition, and data storage was about 35 s for one frequency. Positioning of the finger averaged another 80 s. Thus, the complete tomographic scanning time needed for six fingers and two modulation frequencies was about 15 min.

In the laser scanner unit, the positioning of the finger is carried out by using the mark on the finger as a reference. An additional laser line, across the finger as a pilot beam, helps to find the correct axial position for the mark. The finger is angled parallel to the scanning direction. The scan starts approximately 3 mm before the mark and ends after a distance of 40 mm on both sides. One step of the stepping motor yields a step of the laser line on the finger surface of approximately 0.05 mm and takes about 10 ms. Both cameras are in a free running mode and take images with 30 frames/s. A waiting time of 20 ms is inserted between the steps to get approximately one step per frame. The scanning over 40 mm takes about 25 s, positioning averages another 60 s. Thus the complete time for scanning six fingers is about 7 min.

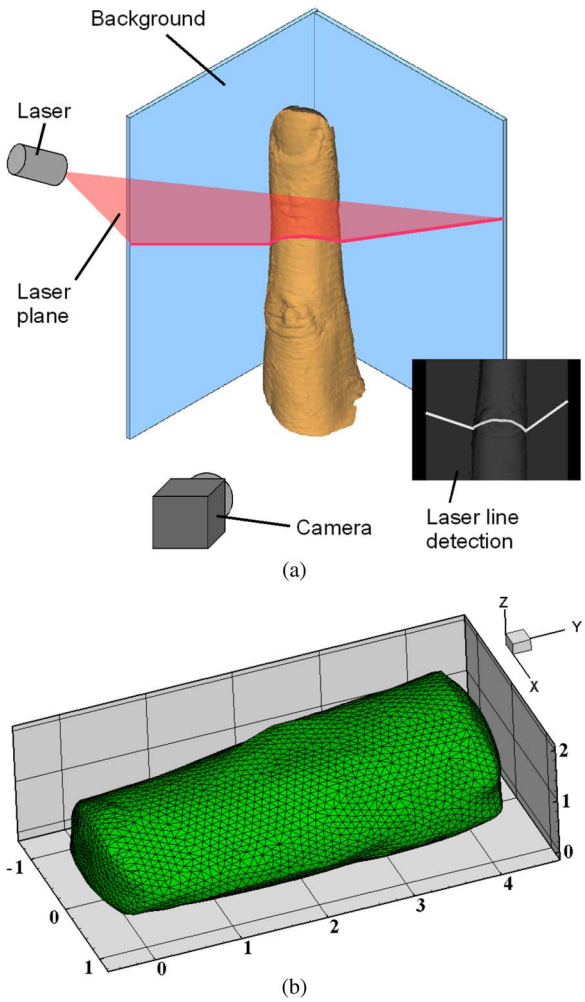

Fig. 4. (a) Surface registration and (b) 3-D mesh generation. The surface scanning unit detects the shape of the laser line on the finger surface and determines the 3-D-surface coordinates while the laser line is scanned over the finger. The background serves for calibration of the camera coordinate system. Surface registration and 3-D mesh generation. (a) 3-D laser scanning to obtain a finger joint geometry and (b) 3-D finite volume mesh generated using the laser scanned surface mesh.

After acquisition, the raw imaging data was processed. In every stack of images a fast Fourier transformation (FFT) was performed through the stack in every pixel. The FFT yielded values for the amplitude, phase and the dc components. By this means 2-D dc, amplitude and phase images were calculated for every distinct source position.

3) Optical Tomographic Reconstruction: Three-dimensional image reconstructions were performed using the PDE-constrained reduced-Hessian SQP method [30], that solves the forward and inverse problems simultaneously. As a forward model this code employs the frequency-domain equation of radiative transfer (FD-ERT) [31], [32]

$$(\nabla\cdot\mathbf{\Omega})\psi(\mathbf{r},\mathbf{\Omega},\omega)+\left(\mu_a+\mu_s+\frac{i\omega}{c}\right)\psi(\mathbf{r},\mathbf{\Omega},\omega)=\frac{\mu_s}{4\pi}\int_{4\pi}\psi(\mathbf{r},\mathbf{\Omega}',\omega)\Phi(\mathbf{\Omega},\mathbf{\Omega}')d\Omega' \quad (1)$$

where $\psi(\mathbf{r},\mathbf{\Omega},\omega)$ is the complex-valued radiance in unit $[\mathrm{W/cm^2/sr.}]$, μ_a and μ_s are the absorption and scattering coefficients, respectively, in units of cm^{-1}, ω is the external source modulation frequency, c is the speed of light inside the medium, and $\Phi(\mathbf{\Omega},\mathbf{\Omega}')$ is the scattering phase function that describes scattering from incoming direction $\mathbf{\Omega}'$ into scattering direction $\mathbf{\Omega}$. In this work we employed the widely used Henyey–Greenstein phase function with $g=0.9$ [33].

Furthermore, to be able to consider the refractive index mismatch at air-tissue interface [34], [35], we implemented a partially-reflective boundary condition

$$\psi_b(\mathbf{r}_b,\mathbf{\Omega},\omega)|_{\mathbf{n}_b\cdot\mathbf{\Omega}<0}=\psi^0(\mathbf{r}_b,\mathbf{\Omega},\omega)+R(\mathbf{\Omega},\mathbf{\Omega}')\cdot\psi_b(\mathbf{r}_b,\mathbf{\Omega}',\omega)|_{\mathbf{n}_b\cdot\mathbf{\Omega}'>0} \quad (2)$$

where $R(\mathbf{\Omega},\mathbf{\Omega}')$ is the reflectivity at Fresnel interface from direction $\mathbf{\Omega}'$ to direction $\mathbf{\Omega}$, $\psi^0(\mathbf{r}_b,\mathbf{\Omega},\omega)$ is the radiation intensity due to the external source function, subscript b denotes the boundary surface of the medium, and $\mathbf{n}_b$ is the unit normal vector pointing outwards at the boundary surface.

Given the spatial distribution of optical properties inside the medium, we solve the radiative transfer equation [(1)] with a discrete ordinates method [34], which provides the prediction of measurements obtained on the surface of the medium $P_{d,s}(\mathbf{r}_b,\omega)=Q_d\psi_s(\mathbf{r}_b,\mathbf{\Omega},\omega)$. Here Q_d is the measurement operator that projects the radiance vector $\psi_s(\mathbf{r}_b,\mathbf{\Omega},\omega)$ of a forward model onto the image plane of a CCD camera.

In PDE-constrained optimization, an image reconstruction problem is to find the radiation intensity vector

$$\psi=(\psi^1,\psi^2,\ldots,\psi^m) \quad (3)$$

and the optical property vector

$$\mu=\left(\mu_a^1,\mu_a^2,\ldots,\mu_a^n,\mu_s^1,\mu_s^2,\ldots,\mu_s^n\right) \quad (4)$$

such that

$$\begin{aligned}\min\quad & f(\mu,\psi)=\frac{1}{2}\sum_{s=1}^{N_s}\sum_{d=1}^{N_d}(Q_d\psi_s-z_{s,d})(Q_d\psi_s-z_{s,d})^*\\ \text{s.t.}\quad & A(\mu_a,\mu_s)\psi_s=b_s;\qquad s=1,\ldots,N_s\end{aligned} \quad (5)$$

where N_s and N_d are the numbers of sources and detectors used for measurements and predictions, $z_{s,d}$, and $Q_d\psi_s$ are the measurements and the predictions for source-detector pairs (s,d) and the operator $()^*$ denotes the complex conjugate of the complex vector.

Given the current estimate of forward and inverse variables (μ^k,ψ^k), the rSQP scheme makes the new iterate for both forward and inverse variables

$$\begin{aligned}\psi^{k+1}&=\psi^k+\alpha^k\Delta\psi^k\\ \mu^{k+1}&=\mu^k+\alpha^k\Delta\mu^k\end{aligned} \quad (6)$$

where a step length α_k provides a sufficient decrease in the l_1 merit function, and a search direction $\Delta p=(\Delta\psi,\Delta\mu)^T$ can be obtained by solving the quadratic programming problem

$$\begin{aligned}\min\quad & \Delta p^{kT}g^k+\frac{1}{2}\Delta p^{kT}W^k\Delta p^k\\ \text{s.t.}\quad & C^{kT}\Delta p^k+(A\psi-b)^k=0.\end{aligned} \quad (7)$$

Here g denotes the gradient of f, W^k denotes the full Hessian (or approximations) of the Lagrangian function $L(\psi, \mu, \lambda) = f(\psi, \mu) + \lambda^T(A\psi - b)$, and C represents the matrix of constraint gradients. A detailed description on the rSQP algorithm can be found in [30].

The code also incorporated the 3-D surface data obtained for each finger, described in Section II-C-1 (also Fig. 4). Using this data, we generated a 3-D finger joint mesh identical to the actual geometry of each finger of interest. A typical 3-D volume mesh was composed of about 30 000 tetrahedron elements. All reconstructions were started with an initial estimate of $\mu_a = 0.3\ \mathrm{cm}^{-1}$ and $\mu_s' = (1-g)\mu_s = 8\ \mathrm{cm}^{-1}$ for all mesh points. Typically, the total reconstruction time was approximately 1–2 h on a computer with an Intel Xeon 3.3 GHz processor.

D. Data Analysis

1) Region of Interest (ROI) and Feature Extraction: After reconstruction of the 3-D spatial distribution of the absorption and scattering coefficients, a 3-D region of interest (ROI) was determined for each finger. In particular, only mesh points that were at least 2 mm away from a tissue boundary were considered to eliminate any reconstruction artifacts that are at times visible near tissue boundaries. Furthermore, only mesh points that were within the lateral extent of the light illumination points were included in the ROI. Only within this range do the measurements provide useful information for the reconstruction code. An example of a reconstructed finger and the resulting ROI is shown in Fig. 5. For better orientation, we also show a photograph and an MRI image that covers approximately the same area of the joint and finger.

From each 3-D ROI we extracted various feature parameters that we subsequently used for our computer-aided diagnostics. These feature parameters included the maximum $(\max)$ and minimum $(\min)$ of all the absorption and scattering coefficients, μ_a and μ_s, within the ROI. Furthermore, we calculated the ratio of the minimum and maximum (ratio=min/max), and the mean and variance (var) across all pixels in each 3-D volume.

Medical experts diagnosed each RA patient using MRI and ultrasound diagnosis as described in Section II-B, and each volumetric image with derived feature parameters ($\min$, $\max$, ratio, and var) was subsequently labeled as "affected" by RA (group A) or "unaffected" by RA (group U). A third group (group H) was formed, which consists of fingers of healthy persons. In total we had 81 fingers in group A, 18 fingers in group U, and 120 fingers in group H.

2) Classification Methods: The goal of the classification method is to determine if an optical tomographic image belongs to a healthy person or a person with RA. In this study we used the image features described in the Section II-D-1 to make this determination. When only one feature was considered [e.g., $\min(\mu_a)$, $\max(\mu_a)$, $\mathrm{ratio}(\mu_a)$, $\mathrm{var}(\mu_a)$, $\min(\mu_s')$, $\max(\mu_s')$, $\mathrm{ratio}(\mu_s')$, or $\mathrm{var}(\mu_s')$], we calculated the mean and variance across images of the joints of healthy volunteers (group H) and of joints affected by RA (group A). Using a student t-test we derived p-values for each image feature and determined if a statistically significant difference between affected and healthy fingers existed, concerning a particular image feature. In addition, we generated receiver operating characteristic (ROC curve) for all imaging parameters. Therefore, assuming a certain threshold, for example $\min(\mu_a)_{th}$ for $\min(\mu_a)$, we say that all images with $\min(\mu_a) < \min(\mu_a)_{th}$ belong to healthy volunteers, while all other images belong to a person affected by RA.

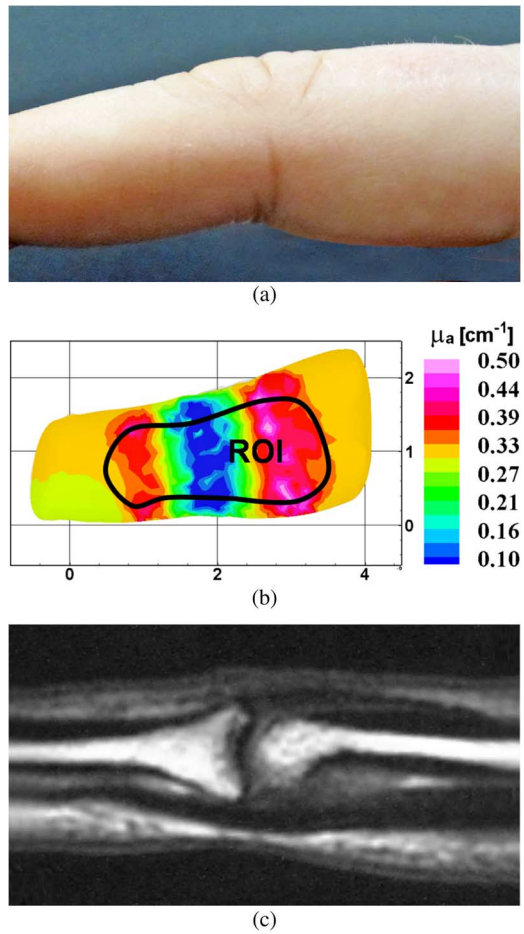

Fig. 5. (a) Photograph showing the approximate range of finger for which the mesh was generate that was used to reconstruct the optical tomographic image. (b) Example of a 2-D cross-section through a 3-D reconstruction of the distribution of the absorption coefficients in a finger joint. Also shown is a selected region of interest (ROI), for which various optical parameters were determined. The ROI was limited to regions at least 2 mm away from boundaries and within the lateral extent of the source and detector placement. (c) For further orientation the corresponding sagittal representation of the MR image is shown.

Based on this classification, we calculated the number of true positive (TP), true negative (TN), false positive (FP), and false negative (FN) classification using our MRI- and US-based ground truth. Given these numbers, we determined the clinically significant values for sensitivity $(Se = \mathrm{TP}/(\mathrm{TP} + \mathrm{FN}))$, specificity $(Sp = \mathrm{TN}/(\mathrm{TN} + \mathrm{FP}))$. By varying the threshold values from 0 to the largest values of $\min(\mu_a)$, we obtained a series of Se and Sp values that are plotted as a ROC curve, which shows Se as a function of $(1 - Sp)$ for the different threshold values. This curve itself can further be described by the area under the curve (AUC) and the Youden (Y) index, which is equivalent to the threshold for which $Y = Se + Sp - 1$ is largest.

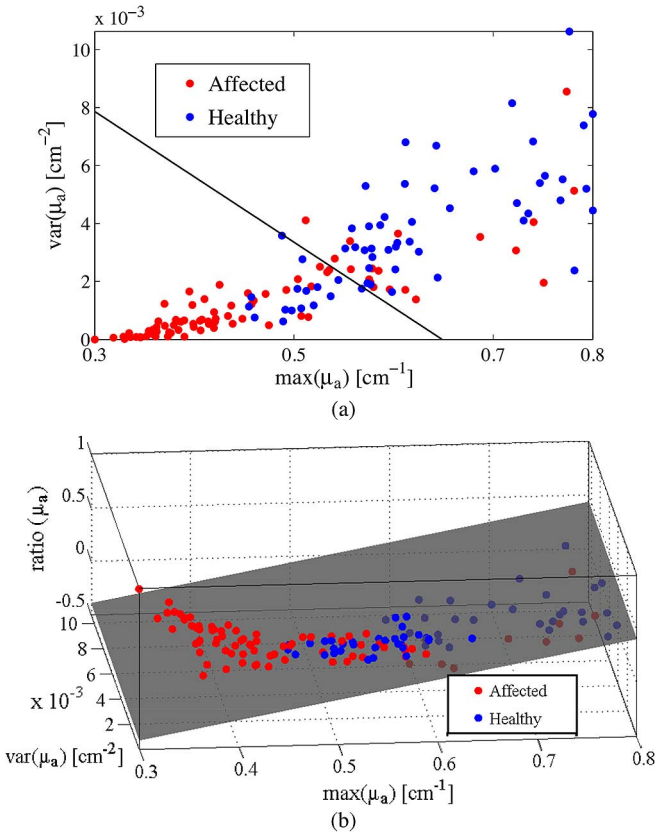

Fig. 6. Examples of (a) 2-D and (b) 3-D feature parameter distributions. The features plotted are $\mathrm{var}(\mu_a)$ and $\max(\mu_a)$ in two dimensions and $\mathrm{ratio}(\mu_a)$, $\mathrm{var}(\mu_a)$ and $\max(\mu_a)$ in three dimensions. Joints affected by RA are shown in red, while healthy joints are plotted in blue. The classification methods used to calculate the line (plane) of separation is LDA.

In addition to comparing Se, Sp, and Y for specific individual image features (e.g., $\min(\mu_a)$, $\max(\mu_a)$, $\mathrm{ratio}(\mu_a)$, $\mathrm{var}(\mu_a)$, $\min(\mu_s')$, $\max(\mu_s')$, $\mathrm{ratio}(\mu_s')$, or $\mathrm{var}(\mu_s')$), we focused on comparing the Se, Sp, and Y derived from combining two or more of these individual parameters. To do so we employed 2-D, 3-D, and 4-D linear discriminant analysis (LDA) [36], [37]. This method creates a separation hyperplane that allows for the classification of a given data point (image) into one of the two classes: here healthy or affected. The classification is made based on the location of a data point relative to the decision boundary (Fig. 6). The calculation of the decision plane in LDA relies on the distance between a given data point and the class centroids. For example, in the 2-D case, where we considered a combination of two image parameters ($\max(\mu_a)$ and $\mathrm{var}(\mu_a)$ in Fig. 6), LDA produces a line as the decision plane [Fig. 6(a)]. Increasing the number of dimensions (i.e., number of image parameters considered) increases the dimensionality of the decision hyperplanes. References for the theoretical development and implementation of LDA can be found in [38] and [39].

In all multidimensional feature classification schemes, we implemented the *leave-p-out* technique for training the classifier (we use $p = 10\%$ throughout this work). This process requires that we randomly selected $(100 - p)\%$ of the data set to calculate the separation line (or hyperplane) as shown in Fig. 6. The remaining $p\%$ of data points are subsequently classified by calculating the TP, FP, TN, FN, Se, Sp, and Y values. In this study we performed this procedure 100 times for each set of features; therefore, 100 times we randomly selected $(100 - p)\%$ of the data set to determine the optimal separation line and used the remaining $p\%$ of the data to calculate the TP, FP, TN, FN, Se, Sp, and Y values. We report the performance of the algorithm by the average values for Se, Sp, and Y over all 100 iterations.

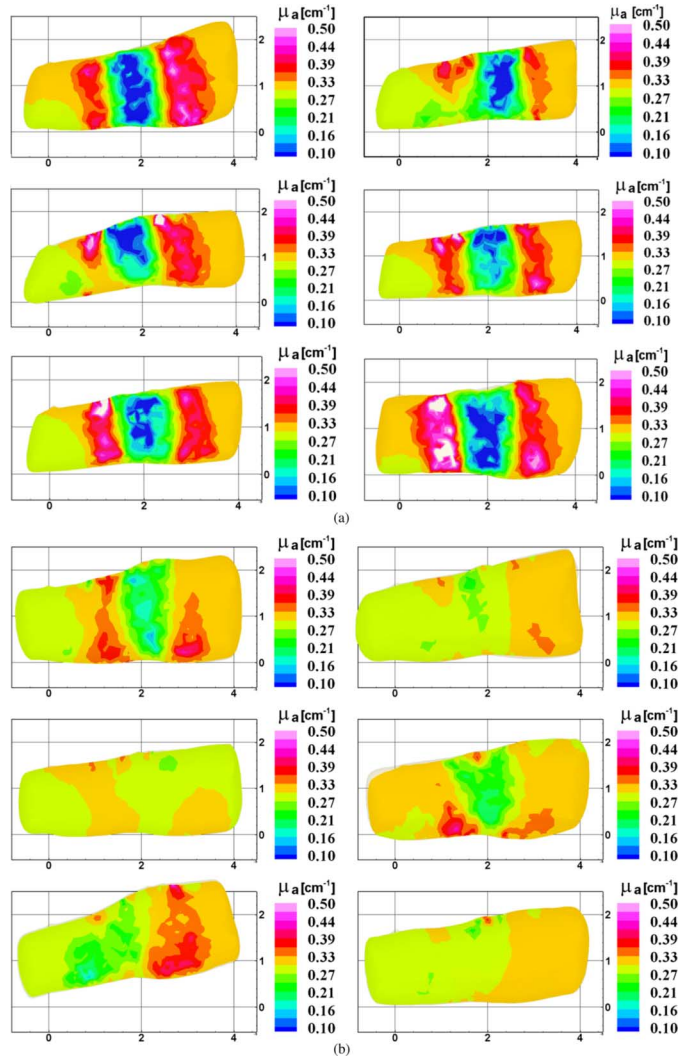

Fig. 7. Examples of 2-D optical tomographic cross-sections through (a) healthy joints and (b) joints affected by RA, showing the spatial distribution of μ_a. Imaging was performed with a source modulation frequency of 600 MHz.

III. Results

A. Introduction

We start by showing examples of 2-D cross-sections through our 3-D tomographic reconstructions of optical properties of healthy fingers and finger affected by RA. Fig. 7 shows images of the absorption coefficient, μ_a, and Fig. 8 shows images of the scattering coefficients, μ_s'. All of theses reconstructions were performed using measurement data obtained at 600 MHz source modulation frequency. In these images the most striking feature is that fingers from healthy volunteers [Fig. 7(a) and Fig. 8(a)] seem to show a larger variation of μ_a and μ_s' values as compared to images of fingers from patients affected by RA [Fig. 7(b) and Fig. 8(b)]. One can also see that images of healthy joints seem

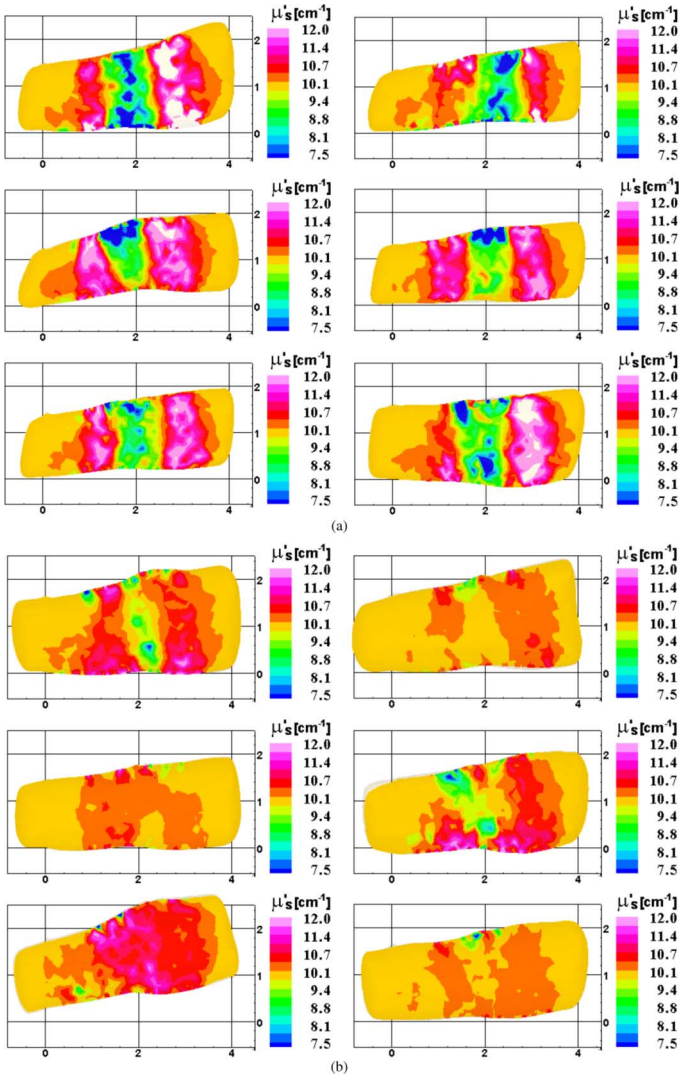

Fig. 8. Examples of 2-D optical tomographic cross-sections through (a) healthy joints and (b) joints affected by RA, showing the spatial distribution of μ_s'. Imaging was performed with a source modulation frequency of 600 MHz.

to show lower μ_a and μ_s' values than joints affected by RA, especially in the region of the joint cavity, in the center of the images. This is in agreement with the well-known fact that the synovial fluid as well as the synovium change their optical properties in patients with RA [40], [41]. The inflammatory process starts in the synovium, leading to changes in tissue architecture and cell structure. Cell proliferation can be observed and the appearance of the synovial fluid changes from a clear, yellowish substance to a turbid, gray-yellowish substance. The number of leukocytes per mL increases from 100–200 in healthy conditions to 1000–100 000 during stages 1 and 2 of the disease. This is particularly important for optical techniques, since leukocytes have a diameter of approximately 7–20 μm and therefore have a considerable effect on the scattering coefficient. Furthermore, the protein content in the synovial fluid approximately triples from 10–20 g/L to 30–60 g/L [42], [43].

To further quantify these findings we started by calculating the mean and standard deviation (std) for min, max, ratio, and var of μ_a and μ_s' for all affected and healthy fingers in this study. The results are summarized in Table I. We found that indeed

TABLE I
MEAN VALUES AND STANDARD DEVIATIONS OF INDIVIDUAL FEATURES

Feature	Healthy Group H Mean ± STD	Affected Group A Mean ± STD	p-value
$max(\mu_a)$	0.62 ± 0.10	0.46 ± 0.12	3.36×10^{-14}
$min(\mu_a)$	0.06 ± 0.05	0.13 ± 0.08	2.01×10^{-7}
$var(\mu_a)$	0.0037 ± 0.0021	0.0014 ± 0.0013	2.30×10^{-13}
$ratio(\mu_a)$	0.11 ± 0.10	0.32 ± 0.25	3.32×10^{-9}
$max(\mu_s')$	11.84 ± 0.12	11.34 ± 0.51	9.21×10^{-12}
$min(\mu_s')$	6.22 ± 1.82	6.86 ± 2.34	0.081
$var(\mu_s')$	0.35 ± 0.17	0.15 ± 0.14	2.71×10^{-12}
$ratio(\mu_s')$	0.53 ± 0.16	0.61 ± 0.22	0.012

Mean and standard deviations of features extracted from OT images of finger joints from groups H and A.

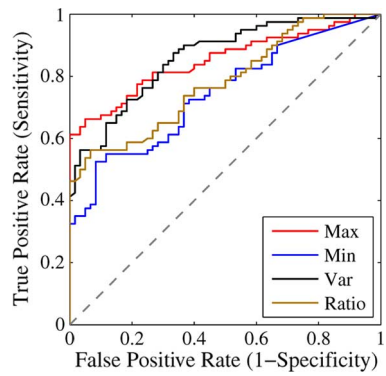

Fig. 9. ROC curves for the features max, min, var, and ratio extracted from μ_a images obtained at 600 MHz.

the differences between healthy and affected joints in $\mathrm{var}(\mu_a)$, $\mathrm{var}(\mu_s')$, and $\mathrm{min}(\mu_a)$ are statistically significant, with p-values of 2.30×10^{-13}, 2.71×10^{-12} and 2.01×10^{-07} respectively. Interestingly all features show statistically significant differences ($p < 0.05$) between images of healthy and affected joints, except for $\mathrm{min}(\mu_s')$ ($p = 0.081 > 0.05$).

Clinically more relevant is an ROC curve analysis. Fig. 9 shows the ROC curves for $\mathrm{min}(\mu_a)$, $\mathrm{max}(\mu_a)$, $\mathrm{ratio}(\mu_a)$, and $\mathrm{var}(\mu_a)$. The area under the curve (AUC) is largest for $\mathrm{var}(\mu_a)$, for which we find $\mathrm{AUC} = 0.882$ compared to $\mathrm{AUC} = 0.865$ for $\mathrm{max}(\mu_a)$. However, $\mathrm{max}(\mu_a)$ yields a slightly higher Youden index $Y = 0.59$ ($Se = 0.81$ and $Sp = 0.78$) than $\mathrm{var}(\mu_a)$ with $Y = 0.58$ ($Se = 0.76$ and $Sp = 0.82$). A similar analysis for μ_s'-dependent features (not shown) results in somewhat lower values for Se, Sp, Y, and AUC.

B. Use of Multiple Parameters

In previous studies we showed that it could be advantageous to combine several of the image features [19], [44], [45]. Table II summarizes the results for absorption and scattering derived image features. Shown are the Se, Sp and Y values as calculated with the LDA method for all possible combinations of parameter pairing. The numbers in bold text indicate the largest Se, Sp, and Y values observed for both absorption and scattering derived parameters. For example, combining $\mathrm{var}(\mu_a)$ with $\mathrm{ratio}(\mu_a)$ resulted in $Y = 0.66$ ($Se = 0.83$, $Sp = 0.83$), which is higher than if $\mathrm{var}(\mu_a)$ is used on its own, for which we had $Y = 0.58$ ($Se = 0.76$ and $Sp = 0.82$) (Fig. 9). When all

TABLE II
LDA CLASSIFICATION RESULTS WITH 600 MHz DATA

Parameter Space	Se	Sp	Y
$max, min\ (\mu_a)$	0.79	0.77	0.56
$max, var\ (\mu_a)$	0.78	0.79	0.58
$max, ratio\ (\mu_a)$	0.80	0.81	0.61
$min, var\ (\mu_a)$	0.78	**0.86**	0.64
$min, ratio\ (\mu_a)$	0.69	0.67	0.36
$var, ratio\ (\mu_a)$	**0.83**	0.83	**0.66**
$max, min, var\ (\mu_a)$	0.78	**0.86**	0.64
$max, min, ratio\ (\mu_a)$	0.79	0.78	0.58
$max, var, ratio\ (\mu_a)$	0.82	0.81	0.63
$min, var, ratio\ (\mu_a)$	0.80	0.84	0.64
$max, min, var, ratio\ (\mu_a)$	0.80	**0.86**	**0.66**
$max, min\ (\mu_s')$	0.92	0.64	0.56
$max, var\ (\mu_s')$	0.76	0.79	0.55
$max, ratio\ (\mu_s')$	**0.93**	0.66	0.59
$min, var\ (\mu_s')$	0.91	0.82	0.73
$min, ratio\ (\mu_s')$	0.67	0.69	0.36
$var, ratio\ (\mu_s')$	0.86	0.74	0.60
$max, min, var\ (\mu_s')$	0.91	**0.86**	**0.76**
$max, min, ratio\ (\mu_s')$	0.92	0.68	0.60
$max, var, ratio\ (\mu_s')$	0.75	0.77	0.52
$min, var, ratio\ (\mu_s')$	0.86	0.82	0.68
$max, min, var, ratio\ (\mu_s')$	0.87	0.83	0.70

Summary of classification results using image features derived from μ_a and μ_s' distributions obtained with imaging data generated at 600 MHz source modulation frequency. The numbers in bold indicated largest values observed.

TABLE III
LDA CLASSIFICATION RESULTS WITH 300 MHz DATA

Parameter Space	Se	Sp	Y
$max, min\ (\mu_a)$	0.78	0.74	0.52
$max, var\ (\mu_a)$	0.74	0.76	0.50
$max, ratio\ (\mu_a)$	0.74	0.78	0.52
$min, var\ (\mu_a)$	**0.80**	0.71	0.51
$min, ratio\ (\mu_a)$	**0.80**	0.70	0.50
$var, ratio\ (\mu_a)$	0.69	0.77	0.46
$max, min, var\ (\mu_a)$	0.76	0.72	0.49
$max, min, ratio\ (\mu_a)$	0.79	0.72	0.51
$max, var, ratio\ (\mu_a)$	0.73	**0.82**	**0.54**
$min, var, ratio\ (\mu_a)$	0.79	0.71	0.50
$max, min, var, ratio\ (\mu_a)$	0.78	0.75	0.53
$max, min\ (\mu_s')$	0.75	0.70	0.45
$max, var\ (\mu_s')$	0.75	0.76	0.51
$max, ratio\ (\mu_s')$	0.58	0.45	0.03
$min, var\ (\mu_s')$	**0.81**	0.74	**0.55**
$min, ratio\ (\mu_s')$	0.68	0.63	0.31
$var, ratio\ (\mu_s')$	0.73	**0.77**	0.50
$max, min, var\ (\mu_s')$	0.73	0.73	0.46
$max, min, ratio\ (\mu_s')$	0.75	0.71	0.47
$max, var, ratio\ (\mu_s')$	0.76	0.76	0.52
$min, var, ratio\ (\mu_s')$	0.72	0.69	0.41
$max, min, var, ratio\ (\mu_s')$	0.72	0.69	0.42

Summary of classification results using image features derived from μ_a and μ_s' distributions obtained with imaging data generated at 300 MHz source modulation frequency. The numbers in bold indicated largest values observed.

four parameters are combined a higher specificity of $Sp = 0.86$ is achieved using LDA, however, Se drops to 0.80, yielding the same $Y = 0.66$.

Combining scattering derived image features resulted in even higher Y, Se, and Sp values. For example, we observed that combining $\max(\mu_s')$, $\min(\mu_s')$, and $\mathrm{var}(\mu_s')$ yields the largest Youden index of $Y = 0.76$ as well as the largest Sp value of $Sp = 0.86$. The highest sensitivity $Se = 0.93$ is reached if $\max(\mu_s')$ is combined with $\mathrm{ratio}(\mu_s')$.

C. Influence of Source-Modulation Frequency

To test the influence of the source modulation frequency on the classification results, we performed the same analysis discussed in Section III-B with data gathered at 0 and 300 MHz. The results are shown in Tables III and IV, respectively. As can be seen for all parameter combinations, the Se, Sp, and Y values are considerably lower when 0 MHz data is used as compared to 300 or 600 MHz data. This clearly supports the hypothesis that frequency-domain data yields better classification results than steady-state data.

Comparing the classification results obtained with the 300 and 600 MHz data, we found that overall Se, Sp and Y values are higher when 600 MHz data is used. (The only exception is the combination of $\min(\mu_a)$ and $\mathrm{ratio}(\mu_a)$, for which at 300 MHz is $Y = 0.5$, while at 600 MHz it is $Y = 0.36$). This is in agreement with our previous findings, which were based on numerical simulations and phantom experiments, that at source modulation frequencies in the range of 400–600 MHz the signal-to-noise level is highest and the resulting image reconstruction are the best for geometries encountered in finger imaging [46], [47].

TABLE IV
LDA CLASSIFICATION RESULTS WITH 0 MHz DATA

Parameter Space	Se	Sp	Y
$max, min\ (\mu_a)$	0.42	0.33	-0.25
$max, var\ (\mu_a)$	**0.55**	**0.46**	**0.01**
$max, ratio\ (\mu_a)$	0.46	0.42	-0.12
$min, var\ (\mu_a)$	0.41	0.37	-0.22
$min, ratio\ (\mu_a)$	0.37	0.35	-0.29
$var, ratio\ (\mu_a)$	0.43	0.37	-0.20
$max, min, var\ (\mu_a)$	0.49	0.40	-0.11
$max, min, ratio\ (\mu_a)$	0.37	0.31	-0.32
$max, var, ratio\ (\mu_a)$	0.52	0.44	-0.04
$min, var, ratio\ (\mu_a)$	0.36	0.33	-0.31
$max, min, var, ratio\ (\mu_a)$	0.48	0.39	-0.14
$max, min\ (\mu_s')$	0.52	0.42	-0.06
$max, var\ (\mu_s')$	0.47	0.43	-0.10
$max, ratio\ (\mu_s')$	0.29	0.46	-0.25
$min, var\ (\mu_s')$	0.59	0.47	0.06
$min, ratio\ (\mu_s')$	0.48	0.44	-0.08
$var, ratio\ (\mu_s')$	0.60	0.52	0.12
$max, min, var\ (\mu_s')$	0.64	0.51	0.15
$max, min, ratio\ (\mu_s')$	0.33	0.40	-0.27
$max, var, ratio\ (\mu_s')$	0.53	0.43	-0.04
$min, var, ratio\ (\mu_s')$	**0.65**	0.53	0.18
$max, min, var, ratio\ (\mu_s')$	0.64	**0.55**	**0.19**

Summary of classification results using image features derived from μ_a and μ_s' distributions obtained with imaging data generated at 0 MHz source modulation frequency. The numbers in bold indicated largest values observed.

D. Comparison of Healthy Joints With Unaffected Joints of RA Patients

So far we have compared images of joints from healthy volunteers and images of affected joints from patients with RA. There is a third group of images, which are images of fingers that belong to patients diagnosed with RA, but that do not show

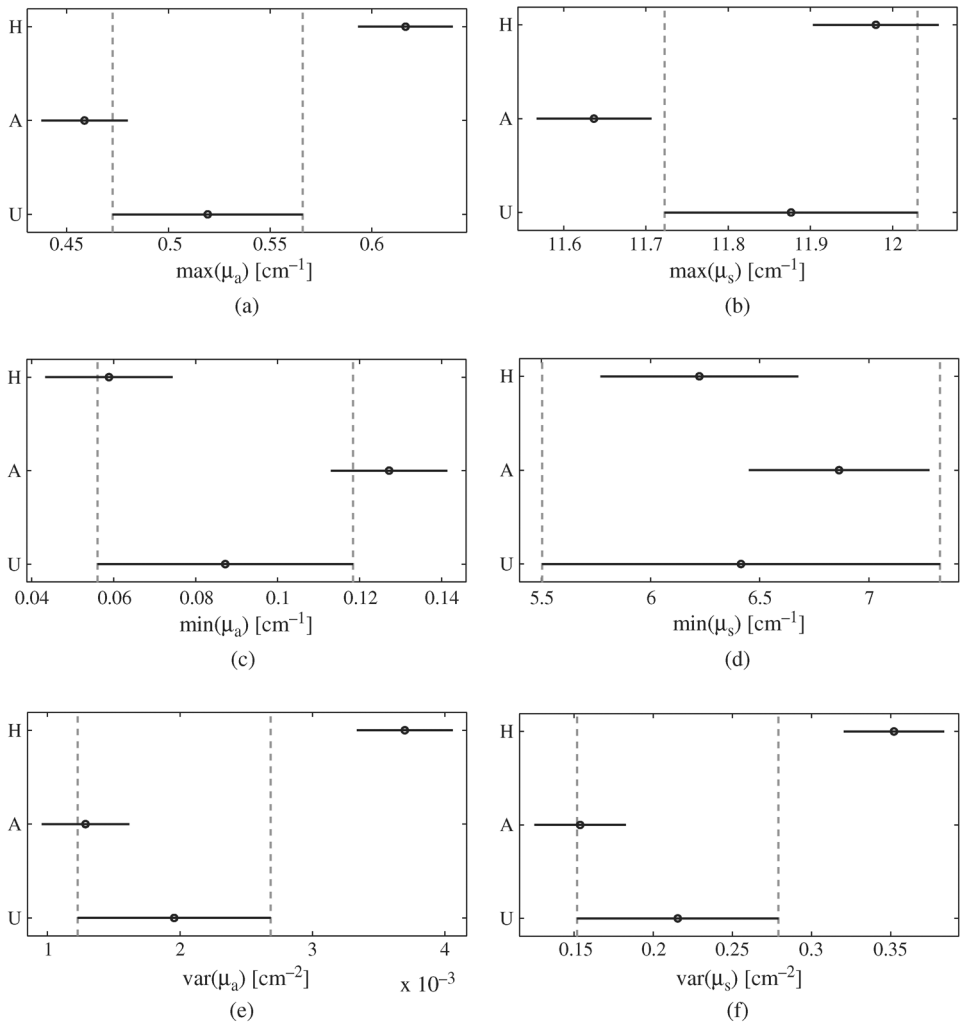

Fig. 10. Mean values with 95% confidence interval of various features extracted from optical tomographic images (600 MHz) of healthy fingers (H), fingers of RA patients that are affected by RA (A), and fingers of RA patient that are unaffected by RA (U) as determined by MRI and US imaging. The left column depicts values extracted from μ_a images, while the column on the right shows values extracted from μ_s' images. The dashed line was plotted to show if there is overlap between the unaffected group U and the affected group A or the healthy group H. If there is no overlap, then the mean of the given feature is different from the other means at statistically significant levels ($p < 0.05$).

any symptoms of RA as determined with MRI and US. Therefore, when MRI or US imaging is performed these fingers look like fingers from healthy persons. To determined how these fingers appear in optical tomographic images, we extracted the previously discussed image features from optical tomographic images of these joints and calculated their respective means, standard errors and 95% confidence intervals. The results are shown in Fig. 10.

Fig. 10 shows the mean and 95% confidence intervals (calculated with an imbalanced one-way ANOVA and using Tukey's test in a multiple comparison procedure) for the means of six different features [$\max(\mu_a)$, $\min(\mu_a)$, $\mathrm{var}(\mu_a)$, $\max(\mu_s')$, $\min(\mu_s')$ and $\mathrm{var}(\mu_s')$] for the healthy joints (H), affected joints of patients with RA (A), and joints not yet affected by RA (U) as determined by MRI and US imaging. We observe that for all features the mean values of the group U lie between the values determined for healthy joints and joints affected by RA. In several cases, the differences are statistically significant. For example for $\mathrm{var}(\mu_a)$, $\mathrm{var}(\mu_s')$, $\max(\mu_a)$, the mean of group U differs significantly from the mean of group H; and for $\max(\mu_s')$ there is a significant difference between group U and group A. ROC analysis for this case yields a sensitivity of $Se = 0.79$ and specificity of $Sp = 0.85$. This suggests that optical tomographic methods may not only be capable of distinguishing between healthy joints and joints of RA patients that are affected by RA, but it may also be more sensitive than MRI or US to see very early changes in joints that do not yet appear to be affected by RA.

Fig. 11 provides another look at this issue. Here we have plotted the combined image features of $\mathrm{var}(\mu_a)$ and $\max(\mu_a)$ for fingers of healthy volunteers (blue dots), finger of RA patients that are affected by RA (red dots), and fingers of RA patients that are not yet affected by RA (white circles), as determined by MR and US imaging. As mentioned before affected joints show smaller variations and maximum absorption coefficient and hence can be predominately found in the lower left corner of this plot, while healthy joints tend to appear in the upper right corner of this plot. Joints of RA patients determined to be yet unaffected (using MRI and US imaging) have a mean that lies between these two classes. Indeed looking at the plot

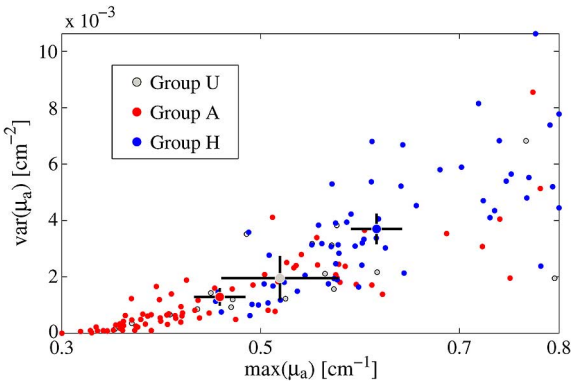

Fig. 11. Distribution of optical tomographic image features found in fingers of healthy volunteers (blue dots), fingers of RA patients that are affected by RA (red dots), and fingers of RA patients that are not yet affected by RA (white circles), as determined by MR and US imaging. The bars show the standard error with respect to $\mathrm{var}(\mu_a)$ and $\max(\mu_a)$, respectively, for each group.

we can see that some joints are clearly with the group of healthy joints, while others fall within the group of affected joints. The later patients may be recommended to start treatment of RA, if studies with a larger number of patients validate these findings.

IV. Conclusion and Summary

In this study we used a new frequency-domain (FD) optical tomography system in conjunction with reduced-spaced quadratic programming algorithm to generate 3-D reconstructions of the optical property distribution in finger joints of healthy volunteers and patients with RA. For a total of 219 fingers we generated 3-D volumetric images of the absorption coefficients, μ_a, and scattering coefficients, μ_s', using experimental data obtained with source modulation frequencies of 0 (continuous wave), 300, and 600 MHz. From each image we extracted various image features such as the largest or smallest coefficients, the ratio of these parameters and variance across the image [$\min(\mu_a)$, $\max(\mu_a)$, $\mathrm{ratio}(\mu_a)$, $\mathrm{var}(\mu_a)$, $\min(\mu_s')$, $\max(\mu_s')$, $\mathrm{ratio}(\mu_s')$, and $\mathrm{var}(\mu_s')$]. Using ultrasound (US) and magnetic resonance (MR) images as gold standard, the 219 fingers were assigned to three different cohorts, including a group of healthy fingers (group H), one groups of joints affected by rheumatoid arthritis (group A), and one group of fingers of RA patients that appeared to be unaffected by RA (group U). Applying classical classification algorithms such as ROC curve analysis and LDA, we explored which image features yield the highest sensitivities and specificities.

In general we found that images generated with 600 MHz data result in better joint classification (higher Se, Sp, and Y) than images generated with continuous wave data (0 MHz) or 300 MHz. This is in agreement with our previous numerical studies that identified modulation frequencies in the range of 400–600 MHz as optimal for finger joint geometries. Furthermore, we found that combining several image features leads to higher Se, Sp and Y values as compared to using only a single feature. For example, combining $\max(\mu_s')$, $\min(\mu_s')$, and $\mathrm{var}(\mu_s')$ leads to $Y = 0.76$ with $Se = 0.91$ and $Sp = 0.86$. The highest sensitivity $Se = 0.93$ is reached if $\max(\mu_s')$ is combined with $\mathrm{ratio}(\mu_s')$. In general it appears that scattering-derived features perform slightly better than absorption-derived features in these multidimensional feature classifications. Furthermore, we observed that the mean of many optical features of joints of patients with RA that seemed to be yet unaffected as determined by US and MR imaging, lies in between values of healthy joints and joints affected by RA. This suggests that optical methods may be useful in diagnosing very early signs of RA in these joints. Larger clinical trials will be necessary to conclusively support this hypothesis.

If the results reported in this study are confirmed in multicenter prospective clinical trials, optical tomographic imaging could play a substantial role in clinical management of RA. Optical tomography has several advantages over MRI as well as US imaging. While MR imaging can provide anatomical features in great detail, it is not typically used for monitoring of RA. The cost related to MR imaging are relatively high and the use of gadolinium as contrast agents is contraindicative in several cases. For example it is well known that gadolinium increases the risk of various kidney diseases. This is a particular problematic for RA patients, since many of the drugs used to treat RA patients can have serious nephrotoxic effects by themselves [48]–[50]. Karie *et al.* recently reported that nearly half of RA patients who participated in their study presented some kidney disease.

Compared to US, optical measurement can be performed contact free. This appears to be an advantage given the increased sensitivity to touch of joints affected by RA and the resulting discomfort experience by patients. Furthermore, the sensitivities and specificities reported in our study compare favorably to a recent finding by Freeston *et al.* [51], who found a sensitivity of 0.71 and specificity of 0.82 using double ultrasound in a study involving 50 patients with RA. Furthermore, it should be noted that in current day-to-day clinical practice, medical imaging techniques are only used for confirmation of the clinical findings. Neither MRI nor US have been elevated to standard of care by the ACR or the EULAR [21]. It remains to be seen if OT can breach that gap. But given the low cost, relatively high sensitivity and specificity, as well as contact and contrast-agent-free measurement approach, it appears that OT could become a valuable tool in the evaluation of rheumatoid arthritis.

References

[1] Y. Xu, N. Iftimia, H. B. Jiang, L. L. Key, and M. B. Bolster, "Imaging of in vitro and in vivo bones and joints with continuous-wave diffuse optical tomography," *Opt. Express*, vol. 8, no. 7, pp. 447–451, 2001.

[2] Y. Xu, N. Iftimia, H. B. Jiang, L. L. Key, and M. B. Bolster, "Three-dimensional diffuse optical tomography of bones and joints," *J. Biomed. Opt.*, vol. 7, no. 1, pp. 88–92, 2002.

[3] Q. Z. Zhang and H. B. Jiang, "Three-dimensional diffuse optical tomography of simulated hand joints with a 64 × 64-channel photodiodes-based optical system," *J. Opt. A: Pure Appl. Opt.*, vol. 7, no. 5, pp. 224–231, 2005.

[4] Q. Z. Zhang and H. B. Jiang, "Three-dimensional diffuse optical imaging of hand joints: System description and phantom studies," *Opt. Lasers Eng.*, vol. 43, no. 11, pp. 1237–1251, 2005.

[5] Z. Yuan, Q. Z. Zhang, E. Sobel, and H. B. Jiang, "Three-dimensional diffuse optical tomography of osteoarthritis: Initial results in the finger joints," *J. Biomed. Opt.*, vol. 12, no. 3, p. 034001, 2007.

[6] Z. Yuan, Q. Zhang, E. S. Sobel, and H. Jiang, "High-resolution x-ray guided three-dimensional diffuse optical tomography of joint tissues in hand osteoarthritis: Morphological and functional assessments," *Med. Phys.*, vol. 37, no. 8, pp. 4343–4354, 2010.

[7] J. Xiao, L. Yao, Y. Sun, E. S. Sobel, J. He, and H. Jiang, "Quantitative two-dimensional photoacoustic tomography of osteoarthritis in the finger joints," *Opt. Express*, vol. 18, no. 14, pp. 14359–14365, 2010.

[8] Z. Yuan, Q. Z. Zhang, E. Sobel, and H. B. Jiang, "Comparison of diffusion approximation and higher order diffusion equations for optical tomography of osteoarthritis," *J. Biomed. Opt.*, vol. 14, no. 5, p. 054013, 2009.

[9] X. D. Wang, D. L. Chamberland, and D. A. Jamadar, "Noninvasive photoacoustic tomography of human peripheral joints toward diagnosis of inflammatory arthritis," *Opt. Lett.*, vol. 32, no. 20, pp. 3002–3004, 2007.

[10] X. D. Wang, D. L. Chamberland, P. L. Carson, J. B. Fowlkes, R. O. Bude, D. A. Jamadar, and B. J. Roessler, "Imaging of joints with laser-based photoacoustic tomography: An animal study," *Med. Phys.*, vol. 33, no. 8, pp. 2691–2697, 2006.

[11] L. L. Gompels, N. H. Lim, T. Vincent, and E. M. Paleolog, "In vivo optical imaging in arthritis—An enlightening future?," *Rheumatology*, vol. 49, pp. 1436–1446, 2010.

[12] S. Biswal, D. L. Resnick, J. M. Hoffman, and S. S. Gambhir, "Molecular imaging: Integration of molecular imaging into the musculoskeletal imaging practice," *Radiology*, vol. 244, no. 3, pp. 651–671, 2007.

[13] M. H. Brern, P. M. Schlechtweg, J. MacKenzie, C. S. Winalski, and P. Lang, "Molecular imaging: Future uses in arthritis," *Radiology*, vol. 46, no. 5, pp. 394–402, 2006.

[14] M. P. M. van der Linden, R. Knevel, T. W. J. Huizinga, and A. H. M. van der Helm-van Mil, "Classification of rheumatoid arthritis," *Arthritis Rheum.*, vol. 63, no. 1, pp. 37–42, 2011.

[15] E. Myasoedova, C. S. Crowson, H. M. Kremers, T. M. Therneau, and S. E. Gabriel, "Is the incidence of rheumatoid arthritis rising?," *Arthritis Rheum.*, vol. 62, no. 6, pp. 1565–1567, 2010.

[16] A. H. Hielscher, A. D. Klose, A. Scheel, B. Moa-Anderson, M. Backhaus, U. Netz, and J. Beuthan, "Sagittal laser optical tomography for imaging of rheumatoid finger joints," *Phys. Med. Biol.*, vol. 49, no. 7, pp. 1147–1163, 2004.

[17] A. K. Scheel, M. Backhaus, A. D. Klose, B. Moa-Anderson, U. J. Netz, K. G. A. Hermann, J. Beuthan, G. A. Müller, G. R. Burmester, and A. H. Hielscher, "First clinical evaluation of sagittal laser optical tomography for detection of synovitis in arthritic finger joints," *Ann. Rheum. Dis.*, vol. 64, pp. 239–245, 2005.

[18] O. Minet, U. Zabarylo, and J. Beuthan, "Deconvolution of laser based images for monitoring rheumatoid arthritis," *Laser Phys. Lett.*, vol. 2, no. 11, pp. 556–563, 2005.

[19] C. D. Klose, A. D. Klose, U. Netz, J. Beuthan, and A. H. Hielscher, "Multi-parameter classifications of optical tomographic images," *J. Biomed. Opt.—Lett.*, vol. 13, no. 5, p. 050503, 2008.

[20] K. Ren, G. Abdoulaev, G. Bal, and A. H. Hielscher, "Frequency-domain optical tomography based on the equation of radiative transfer," *SIAM J. Sci. Comput.*, vol. 28, no. 4, pp. 1463–1489, 2006.

[21] D. Aletaha *et al.*, "2010 rheumatoid arthritis classification criteria," *Arthritis Rheum.*, vol. 62, no. 9, pp. 2569–2581, 2010.

[22] F. C. Arnett, S. M. Edworthy, D. A. Bloch, D. J. McShane, J. F. Fries, and N. S. Cooper *et al.*, "The American Rheumatism Association 1987 revised criteria for the classification of rheumatoid arthritis," *Arthritis Rheum.*, vol. 31, pp. 315–324, 1988.

[23] D. M. van der Heijde, M. A. van't Hof, P. L. van Riel, L. A. Theunisse, E. W. Lubberts, M. A. van Leeuwen, M. H. van Rijswijk, and L. B. van de Putte, "Judging disease activity in clinical practice in rheumatoid arthritis: First step in the development of a disease activity score," *Ann. Rheum. Dis.*, vol. 49, pp. 916–920, 1990.

[24] M. Ostergaard, C. Peterfy, P. Conaghan, F. McQueen, P. Bird, B. Ejbjerg, R. Shnier, P. O'Connor, M. Klarlund, P. Emery, H. Genant, M. Lassere, and J. Edmonds, "OMERACT rheumatoid arthritis magnetic resonance imaging studies. Core set of MRI acquisitions, joint pathology definitions, and the OMERACT RA-MRI scoring system," *J. Rheum.*, vol. 30, no. 6, pp. 1385–1386, 2003.

[25] C. Schirmer, A. K. Scheel, C. E. Althoff, T. Schink, I. Eshed, C. Lembcke, G. R. Burmester, M. Backhaus, B. Hamm, and H. K. Hermann, "Diagnostic quality and scoring of synovitis, tenosynovitis and erosions in low-field MRI of patients with rheumatoid arthritis: A comparison with conventional MRI," *Ann. Rhem. Dis.*, vol. 66, pp. 522–529, 2007.

[26] H. A. Fuchs, R. H. Brooks, L. F. Callahan, and T. Pincus, "A simplified 28-joint quantitative articular index in rheumatoid arthritis," *Arthritis Rheum.*, vol. 32, pp. 531–537, 1989.

[27] M. L. Prevoo, M. A. Vanthof, H. H. Kupper, M. A. Vanleeuwen, L. B. A. Vandeputte, and P. L. C. M. Vanriel, "Modified disease activity scores that include 28 joint counts:—Development and validation in a prospective longitudinal study of patients with rheumatoid arthritis," *Arthritis Rheum.*, vol. 38, no. 1, pp. 44–48, 1995.

[28] M. Szkudlarek, M. Court-Payen, S. Jacobsen, M. Klarlund, H. S. Thomsen, and M. Ostergaard, "Interobserver agreement in ultrasonography of the finger and toe joints in rheumatoid arthritis," *Arthritis Rheum.*, vol. 48, pp. 995–962, 2003.

[29] U. J. Netz, J. Beuthan, and A. H. Hielscher, "Multipixel system for gigahertz frequency-domain optical imaging of finger joints," *Rev. Sci. Instrum.*, vol. 79, no. 8, p. 034301, 2008.

[30] H. K. Kim and A. H. Hielscher, "A PDE-constrained SQP algorithm for optical tomography based on the frequency-domain equation of radiative transfer," *Inverse Problems*, vol. 25, p. 015010, 2009.

[31] K. Ren, G. Bal, and A. H. Hielscher, "Frequency domain optical tomography based on the equation of radiative transfer," *SIAM J. Sci. Comp.*, vol. 28, pp. 1463–1489, 2006.

[32] H. K. Kim and A. Charette, "A sensitivity function-based conjugate gradient method for optical tomography with the frequency-domain equation of radiative transfer," *J. Quant. Spec. Rad. Trans.*, vol. 104, pp. 24–39, 2007.

[33] L. G. Henyey and J. L. Greenstein, "Diffuse radiation in the galaxy," *Astrophysics*, vol. 90, p. 70, 1941.

[34] A. D. Klose, U. J. Netz, J. Beuthan, and A. H. Hielscher, "Optical tomography using the time-independent equation of radiative transfer—Part 1: Forward model," *J. Quant. Spec. Rad. Trans.*, vol. 72, pp. 691–713, 2002.

[35] F. M. Modest, *Radiative Heat Transfer*. New York: McGraw-Hill, 2003.

[36] S. J. Dixon and R. G. Brereton, "Comparison of performance of five common classifiers represented as boundary methods: Euclidean distance to centroids, linear discriminant analysis, quadratic discriminant analysis, learning vector quantization and support vector machines, as dependent on data structure," *Chemometrics Intell. Lab. Syst.*, vol. 95, pp. 1–17, 2009.

[37] G. J. McLachlan, *Discriminant Analysis and Statistical Pattern Recognition*. New York: Wiley, 1992.

[38] W. J. Krzanowski, *Principles of Multivariate Analysis*. Oxford, U.K.: Oxford Univ. Press, 1988.

[39] N. Cristianini and J. Shawe-Taylor, *An Introduction to Support Vector Machines*. Cambridge, U.K.: Cambridge Univ., 2000.

[40] V. Prapavat, W. Runge, J. Mans, A. Krause, J. Beuthan, and G. Müller, "Development of a finger joint phantom for the optical simulation of early stages of rheumatoid arthritis," *Biomedizinische Technik*, vol. 42, pp. 319–326, 1997.

[41] V. Prapavat, "Anwendung der experimentellen Systemanalyse zur Informationsgewinnung aus Streulicht im Frühstadium entzündlich-rheumatischer Weränderungen," Ph.D. dissertation, Tech. Univ., Berlin, Germany.

[42] H. Mohamed-Ali, R. W. Hauer, and H. Sorensen, "Morphology and growth behavior of synovial cells in monolayer culture," *Zeitschrift für Rheumatologie*, vol. 50, no. 2, pp. 74–81, 1991.

[43] L. Dahlberg, L. Ryd, D. Heinegard, and L. S. Lohmander, "Proteoglycan fragments in joint fluids," *Acta. Orthop. Scand.*, vol. 63, pp. 417–423, 1992.

[44] C. D. Klose, H. K. Kim, U. J. Netz, S. Blaschke, P. A. Zwaka, G. A. Müller, J. Beuthan, and A. H. Hielscher, "Computer-aided classification of rheumatoid arthritis in finger joints using frequency domain optical tomography," Advanced Biomedical and Clinical Diagnostic Systems VII A. Mahadevan-Jansen, T. Vo-Dinh, and W. S. Grundfest, Eds., SPIE Int. Symp. Biomed. Opt. Proc., vol. 7169, 2009.

[45] C. D. Klose, A. K. Klose, U. Netz, A. K. Scheel, J. Beuthan, and A. H. Hielscher, "Computer-aided interpretation approach for multi-dimensional optical tomographic images," *J. Biomed. Opt.*, vol. 15, p. 066020, 2010.

[46] H. K. Kim, U. J. Netz, J. Beuthan, and A. H. Hielscher, "Optimal source-modulation frequencies for transport-theory-based optical tomography of small-tissue volumes," *Opt. Express*, vol. 16, pp. 18082–18101, 2008.

[47] X. Gu, K. Ren, and A. H. Hielscher, "Frequency-domain sensitivity analysis for small imaging domains using the equation of radiative transfer," *Appl. Opt.*, vol. 46, no. 10, pp. 1624–1632, 2007.

[48] S. Karie, F. Gandjbakhch, N. Janus, V. Launay-Vacher, S. Rozenberg, C. U. Mai Ba, P. Bourgeois, and G. Deray, "Kidney disease in RA patients: Prevalence and implication on RA-related drugs management: The MATRIX study," *Rheumatology*, vol. 47, no. 3, pp. 350–354, 2008.

[49] K. Karstila, M. Korpela, S. Sihvonen, and J. Mustonen, "Prognosis of clinical renal disease and incidence of new renal findings in patients with rheumatoid arthritis: Follow-up of a population-based study," *Clin. Rheumatol.*, vol. 26, no. 12, pp. 2089–2095, 2008.

[50] H. J. Helin, M. M. Korpela, J. T. Mustonen, and A. I. Pasternack, "Renal biopsy findings and clinicopathologic correlations in rheumatoid arthritis," *Arthritis Rheum.*, vol. 38, no. 2, pp. 242–247, 1995.

[51] J. E. Freeston, R. J. Wakefield, P. G. Conaghan, E. M. A. Hensor, S. P. Stewart, and P. Emery, "A diagnostic algorithm for persistence of very early inflammatory arthritis: The utility of power doppler ultrasound when added to conventional assessment tools," *Ann. Rheum. Dis.*, vol. 69, pp. 417–419, 2010.